Geochemistry, Geophysics, Geosystems

RESEARCH ARTICLE
10.1029/2020GC009388

Electrokinetic Contributions to Self-Potential Signals From Magmatic Stressing

Fee Arens[1], Joachim Gottsmann[1], Karen Strehlow[2], James Hickey[3], and Geoff Kilgour[4]

[1]School of Earth Sciences, University of Bristol, Bristol, UK, [2]GEOMAR Helmholtz Center for Ocean Research, Kiel, Germany, [3]Camborne School of Mines, University of Exeter, Cornwall, UK, [4]GNS Science, Wairakei Research Center, Taupo, New Zealand

Key Points:

- Detectable self-potential (SP) and deformation anomalies result from poroelastic responses of volcanic aquifers by subsurface pressurization
- SP amplitudes and their polarity are sensitive to magmatic stressing and pressure source orientation (dike vs. sill)
- Our multiphysics approach provides new insights into pre-eruptive processes

Supporting Information:

- Supporting Information S1

Correspondence to:
F. Arens,
fee.arens@bristol.ac.uk

Citation:
Arens, F., Gottsmann, J., Strehlow, K., Hickey, J. & Kilgour, G. (2020). Electrokinetic contributions to self-potential signals from magmatic stressing. *Geochemistry, Geophysics, Geosystems*, *21*, e2020GC009388. https://doi.org/10.1029/2020GC009388

Received 21 AUG 2020
Accepted 8 NOV 2020

Abstract Pre-eruptive electrical signals at active volcanoes are generally interpreted in terms of electrokinetic processes. Spatio-temporal self-potential (SP) signals can be caused by strain-induced fluid flow in volcanic aquifers, however, previous studies lack the quantitative assessments of these phenomena and the underpinning poroelastic responses. Here we use Finite-Element Analysis to study poroelastic responses induced by subsurface stressing from sill and dike sources by jointly solving for ground displacements, pore pressure, and SP signals. We evaluate the influence of pressure source orientation on the poroelastic response in two different volcanic aquifers (pyroclastic and lava flow) to provide insights on emergent geodetic and SP signals and their sensitivity to governing parameters. Strain-induced SP amplitudes deduced from a reference parameter set vary in both aquifer models and are of negative polarity (−0.35 and −22.6 mV) for a pressurized dike and of positive polarity (+4 and +20 mV) for a pressurized sill. Importantly, we find uniquely different SP and ground displacement patterns from either sill or dike intrusions. Our study shows that SP signals are highly sensitive to the subsurface Young's modulus, streaming potential coupling coefficient and electrical conductivity of the poroelastic domains. For the set of parameters tested, the dike model predicts SP amplitudes of up to −947 mV which are broadly representative of recorded amplitudes from active volcanoes. Our study demonstrates that electrokinetic processes reflect magma-induced stress and strain variations and highlights the potential of joint geodetic and SP studies to gain new insights on causes of volcanic unrest.

Plain Language Summary Prior to a volcanic eruption a variety of geochemical and geophysical precursors may occur. For example, the subsurface accumulation of magma can result in volcano uplift. Pressure changes associated with the arrival of new magma can cause fluid flow in aquifers and generate a naturally occurring electrical signal. Here we use computer models to study whether electrical signals can be used to determine the processes behind magma accumulation. We find that the electrical signals mirror patterns of volcano deformation signals with distinct patterns for different storage geometries (vertical vs. horizontal storage). Predicted values of signals are similar to those measured at active volcanoes. This indicates that our multiphysical approach provides insights into subsurface processes beneath active volcanoes prior to an eruption.

1. Introduction

Volcanic unrest is often accompanied by anomalous geophysical and geochemical signals that are generally attributed to processes within the subvolcanic plumbing system (Salvage et al., 2017). Precise eruption forecasting remains a key issue in volcanology and depends on the correlation of volcanic precursors to subsurface causative mechanisms (Magee et al., 2018; Sparks, 2003). A major challenge in volcano monitoring is to establish whether a period of volcanic unrest will culminate in an eruption or wane without eruptive activity (Gottsmann et al., 2017; Phillipson et al., 2013; Sparks et al., 2012).

Volcano deformation is a prevalent observable during volcanic unrest (Sparks et al., 2012) caused by pressure changes in the magma reservoir (Lisowski, 2006). Geodetic modeling exploits observed surface displacement to constrain source properties (e.g., pressure changes) and mechanisms driving unrest periods (e.g., Delgado et al., 2018; Gottsmann, Biggs et al., 2020; Head et al., 2019; Hickey et al., 2016).

Volcanic aquifers are sensitive to magmatic stressing which manifests as pore pressure variations and head changes (Newhall et al., 2001). For instance, well-level changes prior to the volcanic eruption of

Usu in 2000 has been ascribed to strain-induced groundwater flow caused by an inflating magma reservoir (Shibata & Akita, 2001). This phenomenon has been observed at several volcanoes (e.g., Mayon, Sakurajima, Vesuvius; Newhall et al., 2001, and references therein) and is generally known as poroelasticity due to the coupling between solid deformation and fluid flow (Wang, 2000).

It is widely recognized that the electrical self-potential (SP) method is sensitive to subsurface fluid flow in aquifers and hydrothermal systems (e.g., Corwin & Hoover, 1979; Revil et al., 2012). SP anomalies in volcanic areas show a recognizable feature known as volcano-electric effect (positive SP anomalies above the volcanic summit; Revil, Saracco et al., 2003) resulting from upwards migrating hydrothermal fluid (Zlotnicki & Nishida, 2003) or from a conductive structure beneath the crater (Ishido, 2004). The SP method is a powerful tool to map hydrothermal systems and morphological features of volcanoes (e.g., Barde-Cabusson et al., 2014; Revil et al., 2011; Villasante-Marcos et al., 2014) but also to monitor volcanic activity (Zlotnicki, 2015). Anomalous electrical signals have been observed during periods of volcanic unrest at several volcanoes (Hashimoto & Tanaka, 1995; Zlotnicki et al., 2001, 2005) and even appear prior to other geophysical signals (e.g., seismicity; Zlotnicki, 2015, and references therein). SP tomography and 3D time-lapse inversion algorithms can accurately identify water flow patterns and SP source locations if the subsurface resistivity structure is known (e.g., Crespy et al., 2008; Jardani et al., 2008, 2007) with application to active volcanic systems (e.g., Vulcano [Revil et al., 2008] and Tongariro [Miller et al., 2018]).

SP measurements are inexpensive, non-intrusive, and efficient (Nyquist & Corry, 2002). The link between electrokinetic processes and solid deformation has already been approached theoretically (Revil, 2007), numerically (Mahardika et al., 2012; Revil & Mahardika, 2013), and tested in a sandbox experiment (Crespy et al., 2008). However, the use of SP anomalies for interrogating volcanic unrest phenomena from strain-induced fluid flow has not yet been tackled. Here we develop a suite of novel numerical models solving for poroelastic effects due to magmatic stressing to jointly and simultaneously evaluate resultant geodetic and SP signals from fluid flow in volcanic aquifers.

2. Methods

2.1. Poroelasticity

Poroelasticity describes the interaction between an elastically deforming solid and fluid flow (e.g., Wang, 2000; see Appendix A for constitutive equations). In a poroelastic medium, fluid absorbs stresses from solid mechanics, which in turn drives fluid flow. The fluid translates changes in volumetric strain (Equation A4) to pore pressure. Compression (decrease in pore space) is accompanied by an increase in pore pressure, dilation by a decrease. As a result fluid can either be expelled from or pulled into a porous media by compression or dilation, respectively (Comsol, 2008; Wang, 2000).

2.2. Self-Potential

The electrical SP is a naturally occurring electrical potential difference (Sill, 1983). The most important source mechanisms in volcanic areas are assigned to the electrokinetic, electrochemical, and thermoelectric effect (e.g., Michel & Zlotnicki, 1998). Electrokinetic processes are caused by fluid flow through a porous media in response to a hydraulic pressure gradient (e.g., pore pressure variations). This gives rise to the streaming potential, provided the presence of the electrical double layer (EDL) (Figure 1). The EDL forms in the pore fluid within a fluid-saturated porous media and is divided into the immobile Stern and mobile diffuse layer. Ions in the Stern layer are adsorbed to the mineral boundary to balance the electric charged grain surface which can develop from chemical reactions with the pore fluid. Excess charge (ionic charges of both polarities) accumulates in the diffuse layer which can be mobilized and transported with the fluid, generating a streaming current and consequently a SP signal (e.g., Revil & Florsch, 2010; Revil et al., 2012; Revil, Naudet et al., 2003). In this study, we focus exclusively on SP signals resulting from electrokinetic processes (see Appendix B for theoretical background).

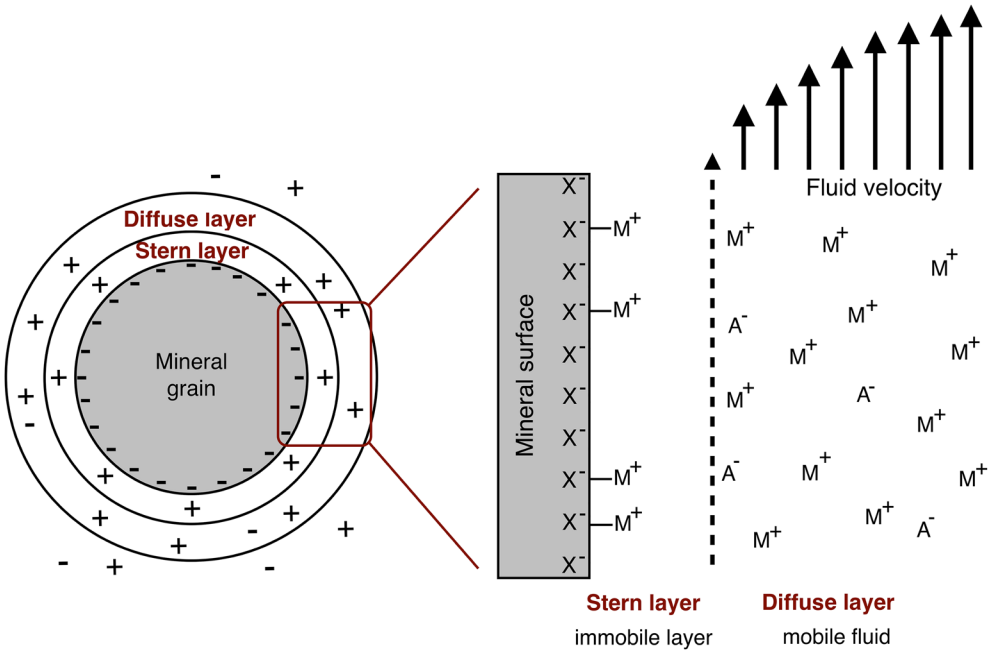

Figure 1. Simplified illustration of the electrical double layer in a fluid-saturated porous media. A mineral grain can develop a surface charge (negative ions, X^-) due to chemical reactivity with the pore water. This is balanced by positive ions (M^+, counterions) within the pore fluid, forming the immobile Stern layer. The remainder of counter- and co-ions (A^-, negative ions) aggregate within the mobile diffuse layer as excess charge, which can be transported with the fluid in the presence of a pressure gradient. In the left figure, counterions and co-ions are represented as positive (+) and negative (−) charge, respectively. Figure modified after Revil and Florsch (2010).

2.3. Model Setup

We use COMSOL Multiphysics (v5.3) to develop a suite of finite-element (FE) forward models that solve for solid mechanics, poroelasticity, and electrokinetic processes. Figure 2 illustrates the model setup including an overview of material properties and applied boundary conditions. We utilize a 2D model geometry with horizontal extent of 100 km in x-direction and vertical dimension of 50 km (z) to construct a layered, heterogeneous model space consisting of host rock (bottom), aquifer (middle), and cap rock (top). A deforming vertical magmatic intrusion (dike) is embedded in the purely elastic host rock, stressing the overlying domains. A dike promotes the transport of magma from a deep-seated reservoir toward the surface (Gudmundsson, 2012), while dike pressurization results from injection of new magma (Gudmundsson, 2011) provoking vertical opening (Magee et al., 2018). We modify the approach by Hickey & Gottsmann, (2014) and implement the pressurized dike as a Bézier polygon instead of a rectangular cavity to reduce meshing problems, which would occur around the edges when using a cavity. The 5 km long dike top is located at a depth of 4 km below the free surface and centered at $x = 0$ km (Figure 2). We assume instantaneous pressurization, by allocating a stepped overpressure (ΔP) of 10 MPa at $t = 10^{-7}$ d to the boundaries of the Bézier polygon. We apply a free surface boundary condition at the top of the model, roller conditions (free of vertical displacement) at the lateral boundaries, and a fixed constraint at the model bottom. Stress and displacement at the internal boundaries are continuous.

Poroelastic and electrokinetic processes are incorporated within aquifer and cap rock, by manually coupling solid-to-fluid mechanics (Strehlow et al., 2015) and resultant hydroelectric effects (Comsol, 2008). Both domains are assumed to be fully saturated with water, which allows us to use a single-phase fluid. Consequently, no time-dependent saturation from the aquifer into the cap rock is considered for the purpose of simplicity. Incorporating fluid flow in the cap rock allows us to capture potential groundwater flow from the aquifer into the overlying domain. Additionally, pore pressure variations in the cap rock

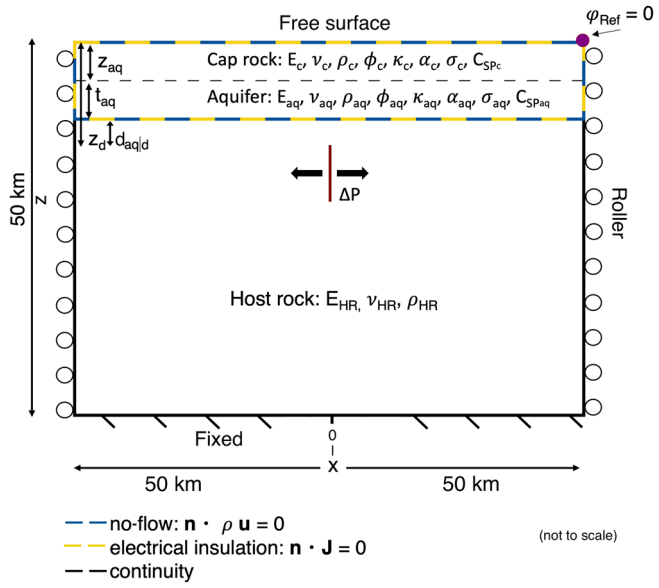

Figure 2. Illustration of the 2D model setup. A boundary load (ΔP) is applied to a vertical polygon at depth. This represents the pressurized dyke which is embedded in a linear elastic host rock. Subsurface strains induce fluid flow in aquifer and cap rock giving rise to an electrical self-potential. There is no fluid flow nor electrical potential outside these domains, while a continuity boundary condition is applied at the internal boundary between cap rock and aquifer. An electrical reference potential of 0 (V) is applied to the top right corner of the cap rock owing the nature of the electrical potential to be a relative measure to a reference point. Boundary conditions for solid mechanics are treated as free surface at the upper boundary, fixed at the bottom, and roller conditions at the lateral boundaries. Stress and displacement at the internal boundaries are continuous. Use Table 1 for symbols and their explanation.

are crucial for superficial SP signals. In our study, we couple electrokinetic processes to the pore pressure gradient, however, streaming current density can also be linked to hydraulic head changes as described by Revil, Naudet et al. (2003). Furthermore, during electrokinetic processes, the generation of the streaming current density induces fluid flow of the opposite direction, which is characterized as electroosmotic drag or flow. This process is of negligible importance in most applications (e.g., Revil, Pezard et al., 1999; Rizzo et al., 2004; Sill, 1983), but was integrated in our numerical models. However, we find that it does not affect the model output significantly.

A no-flow boundary and electrical insulation is applied around both layers, while the internal boundary obeys continuity for fluid flow and streaming current density. A no-flow boundary condition implies fluid flow is confined within the domain with no flow across the boundary. Furthermore, we apply a reference potential of $\varphi_{Ref} = 0$ V to the top right corner of the cap rock owing to the nature of the electrical potential to be a relative measure to a reference point. We set initial pore pressure conditions in both domains as hydrostatic ($p_h = p_f gz$).

In this study, we investigate coupled poroelastic and electrokinetic effects over a time series of 1,000 days and evaluate SP signals and total displacement at the ground surface. Total displacement is given as an absolute value derived from vertical and horizontal displacement.

2.4. Parameterization

We test two distinct reference models (i) a pyroclastic aquifer overlain by a lava flow cap rock (pyroclastic aquifer [PA] model) and (ii) a lava flow aquifer overlain by a pyroclastic cap rock (lava flow aquifer [LFA] model). Aquifer parameterizations are consistent with the nature of aquifers in volcanic areas (Nichols et al., 1996), similar to the approach by Strehlow et al. (2015). Pyroclastic domains are represented by an unconsolidated, mechanically soft pyroclastic material in contrast to the stiff and compact basaltic lava flow deposit. In the latter, porosity is given by connected vesicular pore space. Reference parameters and ranges used in this study are given in Table 1.

Elastic parameters (ν, E) of all domains, except for the pyroclastic layer, are derived using rock density data and equations presented in Brocher (2005). For the host rock, we use typical density values of a granitic crust (Lowrie, 2018), while basalt rock densities are chosen for LFA domains (Gudmundsson, 2011). Elastic properties of the PA domains are chosen according to unconsolidated sand. Poroelastic parameters are required in drained conditions (measured under constant pressure), with little data available for volcanic rocks. Therefore, we use dry elastic values for the poroelastic domains, but allowed a wider range to account for the uncertainty between dry and drained poroelastic values.

Hydraulic and electric parameters are chosen according to basalt (LFA domains) and unconsolidated sand (PA domains). A key parameter in electrokinetics is the streaming potential coupling coefficient (C_{SP}). Although there is discussion in the wider literature on its dependence on material and chemical properties (Jouniaux & Pozzi, 1995; Jouniaux et al., 2000; Revil, Saracco et al., 2003), here we choose C_{SP} accordingly to pore fluid salinity. C_{SP} for groundwater and meteoric water and salinities <1,000 ppm (USGS, 2018) ranges between 10^{-5} and 10^{-7} (V/Pa; Vinogradov et al., 2010). In both models, C_{SP} in aquifer and cap rock is identical. Although we neglect a material-dependence of C_{SP}, the streaming current coupling coefficient L_{SP} is different in both aquifers and cap rocks as the models incorporate distinct variations of the electrical conductivity in the modeling domains (Equation B4).

Table 1
Overview of Parameter Space Used in This Study

Parameter	Domain	Reference value	Range	Reference
Young's modulus	Host rock—E_{HR}	70 GPa	63–80 GPa	Brocher (2005)
Young's modulus pyroclastic	PA aquifer—E_{aq}	25 MPa	10–100 MPa	Gudmundsson (2011); Schön (2011)
	LFA cap rock—E_c			
Young's modulus lava flow	LFA aquifer—E_{aq}	90 GPa	35–127 GPa	Brocher (2005)
	PA cap rock—E_c			
Poisson's ratio	Host rock—ν_{HR}	0.25	Constant	Brocher (2005)
Poisson's ratio pyroclastic	PA aquifer—ν_{aq}	0.3	0.2–0.4	Gudmundsson (2011); Schön (2011)
	LFA cap rock—ν_c			
Poisson's ratio lava flow	LFA aquifer—ν_{aq}	0.26	0.25–0.27	Brocher (2005)
	PA cap rock—ν_c			
Density	Host rock—ρ_{HR}	2,670 kg m^{-3}	2,600–2,700 kg m^{-3}	Lowrie (2018)
Density pyroclastic	PA aquifer—ρ_{aq}	1800 kg m^{-3}	1,400–2,300 kg m^{-3}	Gudmundsson (2011); Schön (2011)
	LFA cap rock—ρ_c			
Density lava flow	LFA aquifer—ρ_{aq}	2,800 kg m^{-3}	2,400–3,000 kg m^{-3}	Gudmundsson (2011); Schön (2011)
	PA cap rock—ρ_c			
Permeability pyroclastic	PA aquifer—κ_{aq}	10^{-11} m^2	10^{-8}–10^{-14} m^2	Freeze and Cherry (1979); Schön (2011); Fetter (2013)
	LFA cap rock—κ_c			
Permeability lava flow	LFA aquifer—κ_{aq}	10^{-12} m^2	10^{-9}–10^{-14} m^2	Freeze and Cherry (1979); Schön (2011); Fetter (2013)
	PA cap rock—κ_c			
Porosity pyroclastic	PA aquifer—ϕ_{aq}	0.35	0.25–0.5	Fetter (2013)
	LFA cap rock—ϕ_c			
Porosity lava flow	LFA aquifer—ϕ_{aq}	0.1	0.01–0.2	Fetter (2013)
	PA cap rock—ϕ_c			
Biot-Willis coefficient pyroclastic	PA aquifer—α_{aq}	0.6	0.6–1	Wang (2000)
	LFA cap rock—α_c			
Biot-Willis coefficient lava flow	LFA aquifer—α_{aq}	0.2	0.2–1	Wang (2000)
	PA cap rock—α_c			
Electrical conductivity pyroclastic	PA aquifer—σ_{aq}	10^{-4} S m^{-1}	10^{-5}–10^{-3} S m^{-1}	Telford et al. (1990); Schön (2011)
	LFA cap rock—σ_c			
Electrical conductivity lava flow	LFA aquifer—σ_{aq}	5×10^{-4} S m^{-1}	10^{-6}–10^{-3} S m^{-1}	Telford et al. (1990); Schön (2011)
	PA cap rock—σ_c			
Streaming potential coupling coefficient	PA/LFA aquifer—C_{SPaq}	-10^{-6} V Pa^{-1}	-10^{-5}–10^{-7} V Pa^{-1}	Vinogradov et al. (2010)
	PA/LFA cap rock—C_{SPc}	C_{SPaq}	Model variant	
Streaming current coupling coefficient	PA/LFA aquifer—L_{SPaq}	$C_{SPaq} \times \sigma_{aq}$	Model variant	Equation B4
	PA/LFA cap rock—L_{SPc}	$C_{SPc} \times \sigma_c$	Model variant	
Water compressibility	χ_f	4×10^{-10} Pa^{-1}	T-dependent (Table S1)	Fetter (2013)
Water density	ρ_f	1,000 kg m^{-3}	T-dependent (Table S1)	Turcotte and Schubert (2002)
Water viscosity	η_f	10^{-3} Pa s	T-dependent (Table S1)	Turcotte and Schubert (2002)
Dike pressurization	ΔP	10 MPa	Constant	Gudmundsson (2011)
Dike top depth	z_d	4 km	2–8 km	-
Distance aquifer dike	$d_{aq/d}$	3 km	1–7 km	-

Table 1 *Continued*

Parameter	Domain	Reference value	Range	Reference
Aquifer top depth	z_{aq}	500 m	100–750 m	-
Aquifer thickness	t_{aq}	500 m	100–750 m	-

Note. Model properties are given for HR, aq, and c for PA and LFA model.
Abbreviations: aq, aquifer; c, cap rock; HR, host rock; LFA, lava flow aquifer; PA, pyroclastic aquifer

2.5. Parametric Study

We perform a Global Sensitivity Analysis (GSA) using the SAFE toolbox (Pianosi et al., 2015) to identify the most influential parameters on key model outputs (wavelength and amplitude of SP signals; see Appendix C for details). We tested 17 selected input parameters and calculated the sensitivity for an ensemble of 540 (given $n = 30$) model runs. The randomly generated sampling matrix is implemented in COMSOL Multiphysics by a parametric sweep. We acknowledge that the randomly selected sampling matrix might include parameter combinations which are physically unrealistic, but essential for the GSA. We test the GSA on elastic, hydraulic, and electric properties. Elastic parameters include the Young's modulus (materials resistance to strain), Poisson's ratio (negative ratio of lateral to longitudinal strain), and the rock density. Permeability, the mobility of water circulation in interconnected voids, porosity (void space), and Biot-Willis coefficient (degree of poroelastic coupling) are grouped into hydraulic parameters. Electrical properties are the electrical conductivity and the streaming potential coupling coefficient, which links pore pressure and electrical potential. Fluid parameters, host rock Poisson's ratio as well as spatial features of aquifer and dike were kept constant during the GSA.

While the streaming coupling coefficient is kept identical in cap rock and aquifer in the GSA, we separately test the influence of cap rocks streaming potential (C_{SPc}) on SP signals. For this, we vary C_{SPc} by ± one order of magnitude relative to reference value $C_{SPRef} = -10^{-6}\left(V / Pa\right)$.

Beside the sensitivity analysis, we test a variety of spatial and thermal parameters and their influence on spatio-temporal SP signals. We evaluate the effect of pressure source orientation between a vertical $\left(\text{dike}, Z_{d_{dike}} = -4\,\text{km}\right)$ and a horizontal intrusion $\left(\text{sill}, Z_{d_{sill}} = -6.5\,\text{km}\right)$ on electrokinetic processes, keeping the center of both intrusions constant at −6.5 km. Additionally, we investigate the influence of varying aquifer thickness (t_{aq}), aquifer depth (z_{aq}) and distance between aquifer and dike ($d_{aq/d}$) on SP signals. When exploring these effects solely one feature is changed at a time, while all others are kept constant. This is done to investigate each spatial effect in isolation and to exclude additional influences.

Moreover, we investigate the effect of temperature on SP signals by integrating temperature-dependent fluid parameters in the top layers. We used Steam97Web (2020) to calculate pore fluids viscosity, compressibility, and density for several temperatures depending on the lithostatic pressure. For the PA model an average lithostatic pressure of 3.7 and 11.2 MPa is used for the cap rock and aquifer, respectively, whilst values of 6.4 MPa (cap rock) and 19.3 MPa (aquifer) are calculated for the LFA model. Table S1 gives an overview of temperature-dependent fluid parameters used in this study. We test (i) the effect of each temperature independently and (ii) a linear heating. The latter is subdivided into rapid and slow heating modes, whereby temperature is increased to 200°C within 10 days (rapid) and 100 days (slow). Note, that changes in temperature and associated fluid properties are varied simultaneously in both the cap rock and the aquifer. Although the sensitivities of temperature-dependent rock properties (e.g., σ) on SP signals are explored as part of the GSA, we do not consider them in the remainder of the models in order to prevent masking of the contribution to SP signals from temperature-dependent pore fluid properties.

3. Results

3.1. Reference Simulations

Figure 3 (panels a and b) show the initial response (expressed at $t = 10^{-5}d = 1s$ throughout this study) after dike pressurization of the reference simulation. A dike provokes a similar superficial V-shape spatial

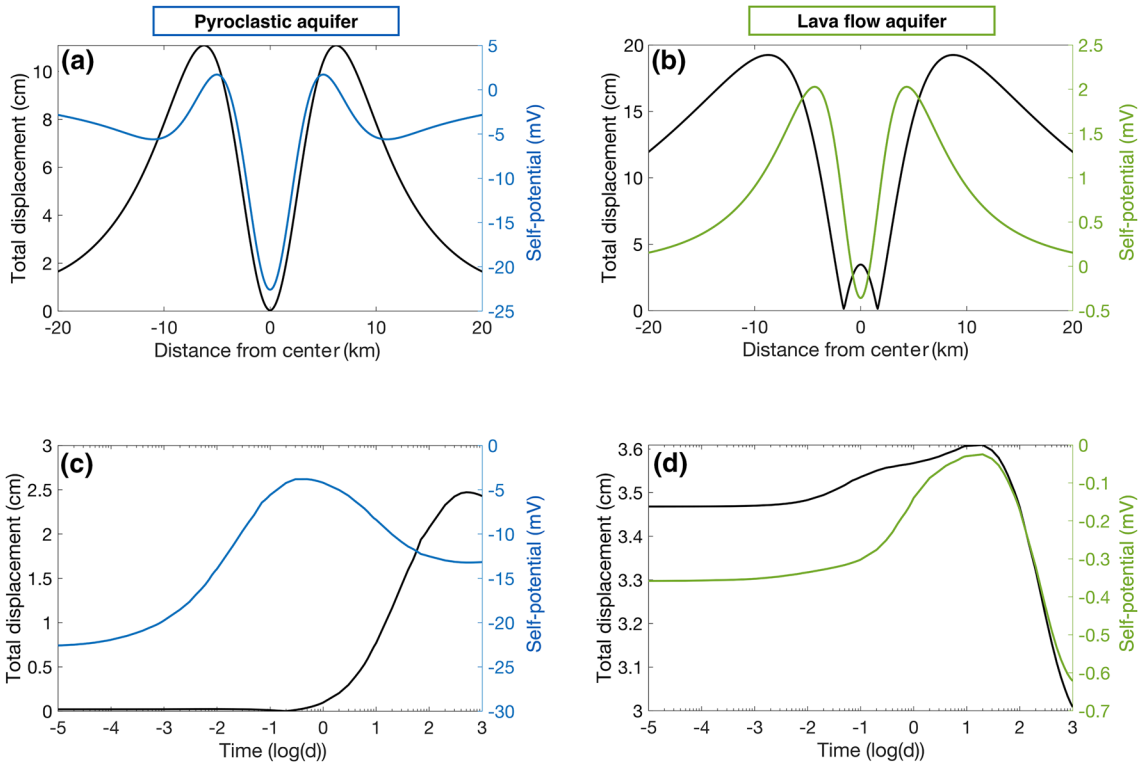

Figure 3. Upper panels (a and b) show the results of the reference simulations along the free surface at $t = 1$ s after dike pressurization for (a) PA and (b) LFA model. SP (right y-axis) and total ground displacement (absolute values, left y-axis) show a V-shape spatial patterns, with minimal values observed directly above the pressure source. Note, that the secondary maximum of total displacement in the LFA model represents ground subsidence in reality. Lower panels (c and d) display the evolution of the SP anomaly and total ground displacement with time (log-scale) at the central superficial point ($x = z = 0$) for (c) PA and (d) LFA model. The amplitude and temporal evolution of total displacement and SP anomaly depends strongly on the domain properties of aquifer and cap rock. LFA, lava flow aquifer; PA, pyroclastic aquifer; SP, self-potential.

pattern for both total displacement and SP anomaly, with minimal values at the center ($x = z = 0$) and a local maximum between 5 and 6 km distance. We observe fundamental differences in the magnitudes of both signals between the PA and the LFA model. Total displacement at the free surface is highest in the LFA model (Figure 3b), with central displacement of 3.4 cm and a vertical uplift of 19 cm at ~5 km distance from the origin. Central SP amplitudes are greatest in the PA model (−22.6 mV) compared to LFA model (−0.35 mV), while the difference in the SP amplitudes at 5 km distance is only 0.3 mV between both models.

The temporal evolution of the SP and total displacement at the central surface point ($x = z = 0$) is shown in Figure 3 (panels c and d). Total displacement in the PA model increases markedly from $\log(t) = 0$ days to a maximum of ~2.4 cm, while displacement in the LFA model peaks at $\log(t) = 1.3$ days, followed by a continuous decrease with time without equilibrating. In contrast to the distinct temporal evolution of the total displacement, the SP signal shows similarities in both models. An initial SP increase within the first minutes to days after the dike intrusion is followed by a continuous decrease in the LFA model, while the SP signal stabilizes around −13 mV ($\log(t)$~2.4 days) in the PA model.

3.2. Sensitivity Analysis

Figure 4 shows the results of the GSA for the reference models at different times after dike pressurization. The sensitivity at five different superficial locations ($z = 0$) between 0 and 20 km from the model center is given by the stacked Elementary Effect Test (EET) mean, which is a measure of the overall influence of an input parameter on the SP signal. In both models, SP signals are spatio-temporally sensitive to elastic properties except for the rock density of all domains. Hydraulic parameters show an initial effect on SP signals

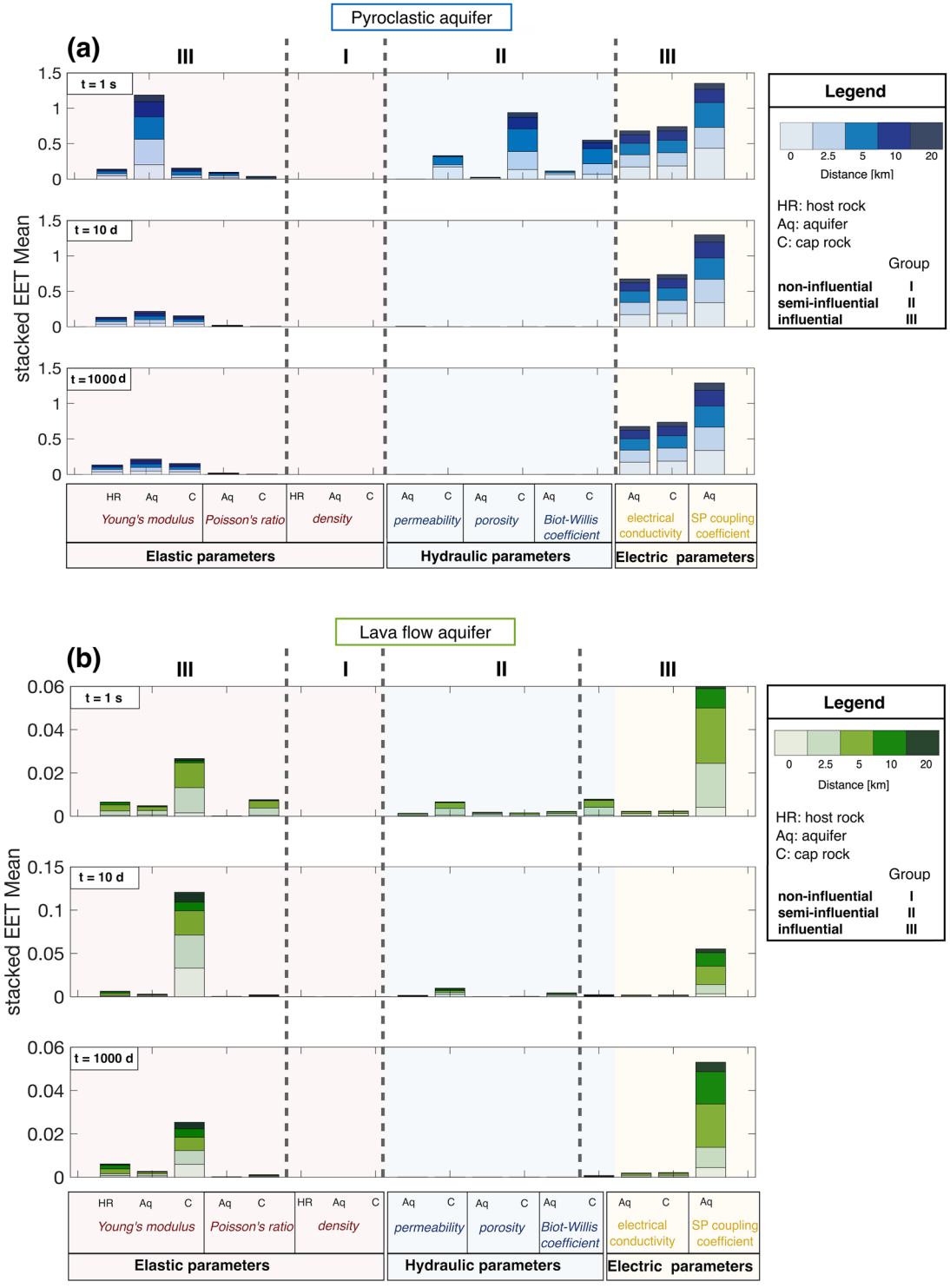

Figure 4. Results of the sensitivity analysis for (a) PA and (b) LFA model at $t = 1$ s, 10 days, 1,000 days after dike pressurization. The sensitivity of 17 model parameters on SP signals is evaluated. Colored bars represent the sensitivity by the stacked EET (y-axis) mean. Sensitivity at five different locations from the model center ($x = 0$, 2.5, 5, 10, 20 km; $z = 0$) are displayed. Input parameters are grouped in elastic (red), hydraulic (blue), and electric (yellow) properties along the x-axis. Parameter space is categorized into non-influential (I), semi-influential (II), and influential (III) effect on SP signals. Stacked sensitivity values of negligible parameters are $\leq 0.1\%$ of the maximum stacked EET means, which are 1.35 (PA) and 0.12 (LFA), respectively. While influential parameters affect the SP signal throughout time, semi-influential parameters show the highest effect after the initial response but becomes non-influential with time. For example, porosity of the cap rock (a; group II) has a significant influence on SP signals at $t \leq 10$ days, yet, negligible sensitivity at $t = 1{,}000$ days. EET, Elementary Effect Test; LFA, lava flow aquifer; PA, pyroclastic aquifer; SP, self-potential.

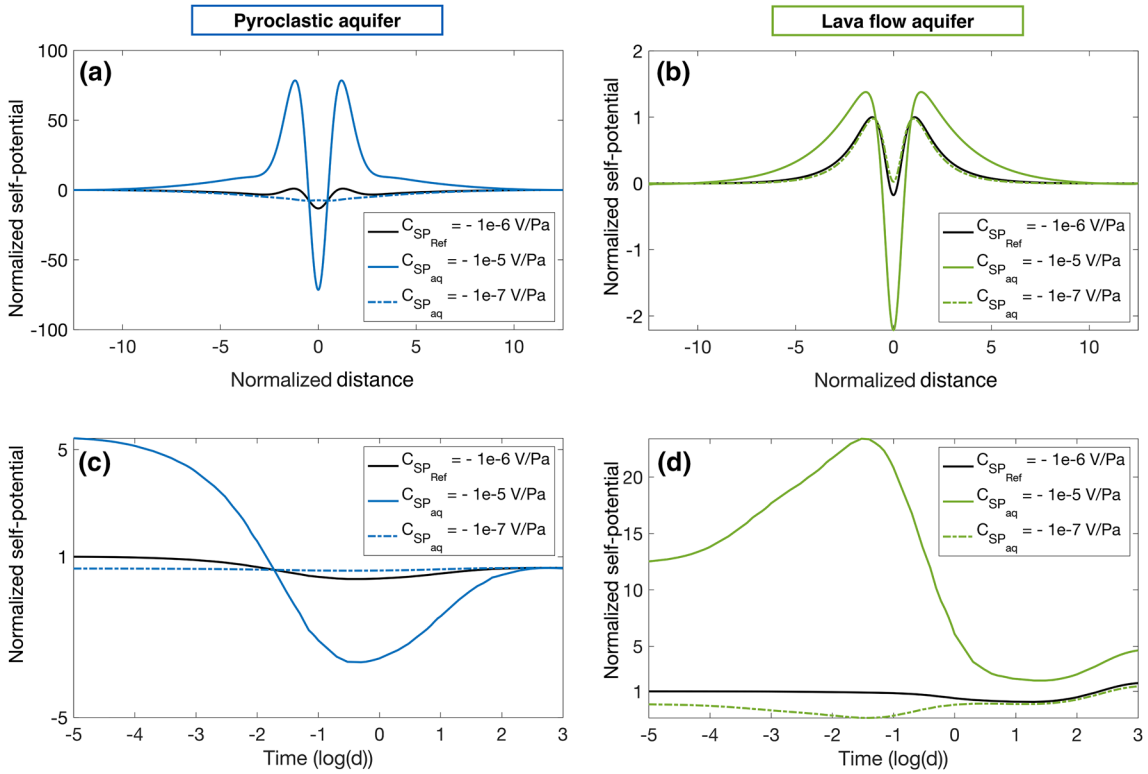

Figure 5. Influence of cap rock streaming potential coupling (C_{SPc}) on the SP signal, while keeping aquifer values constant ($C_{SPaq} = -10^{-6}$ (V/Pa)). Upper panels show the normalized SP signal along the ground surface (distance normalized to dike depth at 4 km) at $t = 1$s for (a) PA and (b) LFA model. SP is normalized to maximal values of the reference simulations ($SP_{PA} = 1.7$ mV, $SP_{LFA} = 2$ mV). The C_{SPc} value controls the magnitude of the SP signal, with greatest variations of ~78 (PA) and ~1.4 (LFA) relative to the maximal SP_{Ref} values. Lower graphs show the temporal evolution (log-scale) of the SP signal for (c) PA and (d) LFA model at the central surface point ($x = z = 0$). SP values are normalized to $SP_{PA} = -22.6$ mV and $SP_{LFA} = -0.35$ mV at $t = 1$ s and are of positive polarity for SP variations <0 relative to SP_{Ref}. LFA, lava flow aquifer; PA, pyroclastic aquifer; SP, self-potential.

after source pressurization, which diminishes with time apart from Biot-Willis coefficient of the cap rock (LFA model). The influence of hydraulic parameters on SP signals decrease markedly in the first 10 days after source pressurization in the PA model compared to the LFA model. Electric parameters show an overall influence on SP signals throughout time in both models with values comparable to elastic properties.

3.3. Cap Rock Streaming Potential Coupling Coefficient (C_{SPc})

Figure 5 shows the influence of varying cap rock streaming potential coupling coefficient (C_{SPc}) on the SP anomaly, while keeping aquifer values constant at $C_{SPaq} = -10^{-6}(\mathrm{V/Pa})$. For the largest value tested ($C_{SPc} = -10^{-5}(\mathrm{V/Pa})$), we observe SP anomalies amplified by up to a factor of ~78 times greater than that of the maximal SP_{Ref} value in the PA model. The SP signal shows greatest spatio-temporal SP deviations from the reference simulations with time for ($C_{SPc} = -10^{-5}(\mathrm{V/Pa})$), while SP amplitudes remain broadly unchanged for $C_{SPc} < C_{SPRef}$ (Figures 5c and 5d).

3.4. Dike Versus Sill Intrusion

Figure 6 shows the effect of the pressure source orientation (vertical dike or horizontal sill) on SP and ground deformation along the free surface. A pressurized sill provokes a spatial SP and deformation pattern which is inverse to the dike-induced V-shape feature. For a pressurized sill, we observe a central uplift of 5.2 (PA) and 2.8 (LFA) times that of the corresponding maximal reference displacement. A horizontal pressure source produces amplified SP values up to ~19 (PA) and ~3.9 (LFA) times that of maximal SP_{Ref}.

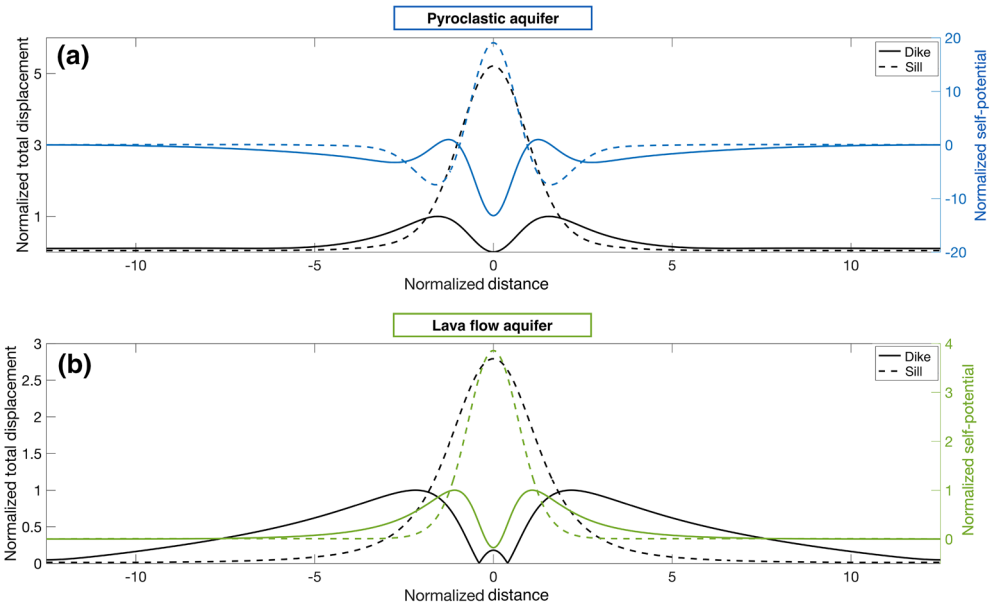

Figure 6. Comparison between normalized superficial SP anomaly and total displacement at $t = 1$ s for (a) PA and (b) LFA model. Results underline the fundamental differences in the spatial SP and deformation pattern between a vertical (solid line) and horizontal pressure source (dashed line). Distance (x-axis) is normalized to the dike depth (4 km). SP and total displacement are normalized to maximal reference values of $SP_{PA} = 1.7$ mV, $SP_{LFA} = 2$ mV, $dis_{PA} = 11$ cm, and $dis_{LFA} = 19$ cm. SP values are of negative polarity for SP variations <0 relative to SP_{Ref}. LFA, lava flow aquifer; PA, pyroclastic aquifer; SP, self-potential.

3.5. Influence of Distance Between Pressure Source and Aquifer

For the case of a pressurized dike, we have tested the influence of its proximity to the aquifer on the SP signal. Higher SP amplitudes correlate with greater proximity of the two domains (Figures 7a and 7b). For the closest distance tested ($d_{aq/d} = 1$ km), we observe maximal SP variations of ∼1.5 (PA) and ∼2 (LFA) relative to the initial SP_{Ref}. SP amplitudes remain broadly unchanged over time for $d_{aq/d} > d_{Ref}$ in comparison to the reference model or $d_{aq/d} < d_{Ref}$.

An increase in aquifer depth and thickness shortens the distance between aquifer and pressure source. For a shallower-seated aquifer with constant thickness ($t_{Ref} = 500$ m), we observe a greater deviation from the reference simulation in the PA model and in particular in the temporal occurrence of the peak amplitude. For the shallow-most aquifer SP signal peaks at $\log(t) = -3$ days compared to $\log(t) \sim 0$ days for deeper aquifers. In the LFA model, the peak amplitude changes compared to the reference model are most significant for the case of the shallow-most aquifer tested in this section. In addition, the SP signal is double-peaked at $\log(t) = 0.5$ days and $\log(t) = 1.5$ days. The temporal evolution of SP amplitudes remains broadly unchanged for deeper-seated aquifers.

Increasing aquifer thickness at constant depth ($z_{Ref} = 500$ m) has minor effects in terms of peak amplitude and its temporal evolution in the LFA model. The SP amplitude deviates markedly from the reference simulation in the PA model for the case of the thinnest aquifer tested.

3.6. Thermal Influence

We have tested the effect of temperature-dependent fluid parameters on the SP signal (Figures 8a and 8b) for the case of a pressurized dike. We observe a change in peak amplitude of ∼0.12 (PA) and ∼0.0009 (LFA) relative to initial SP_{Ref} values for the highest temperature tested. In both models, the temporal occurrence of the peak amplitude deviates from the reference simulations, with earlier peaks for higher temperatures. Figures 8c and 8d show the influence of linear heating on the SP signal, where aquifer and cap rock are

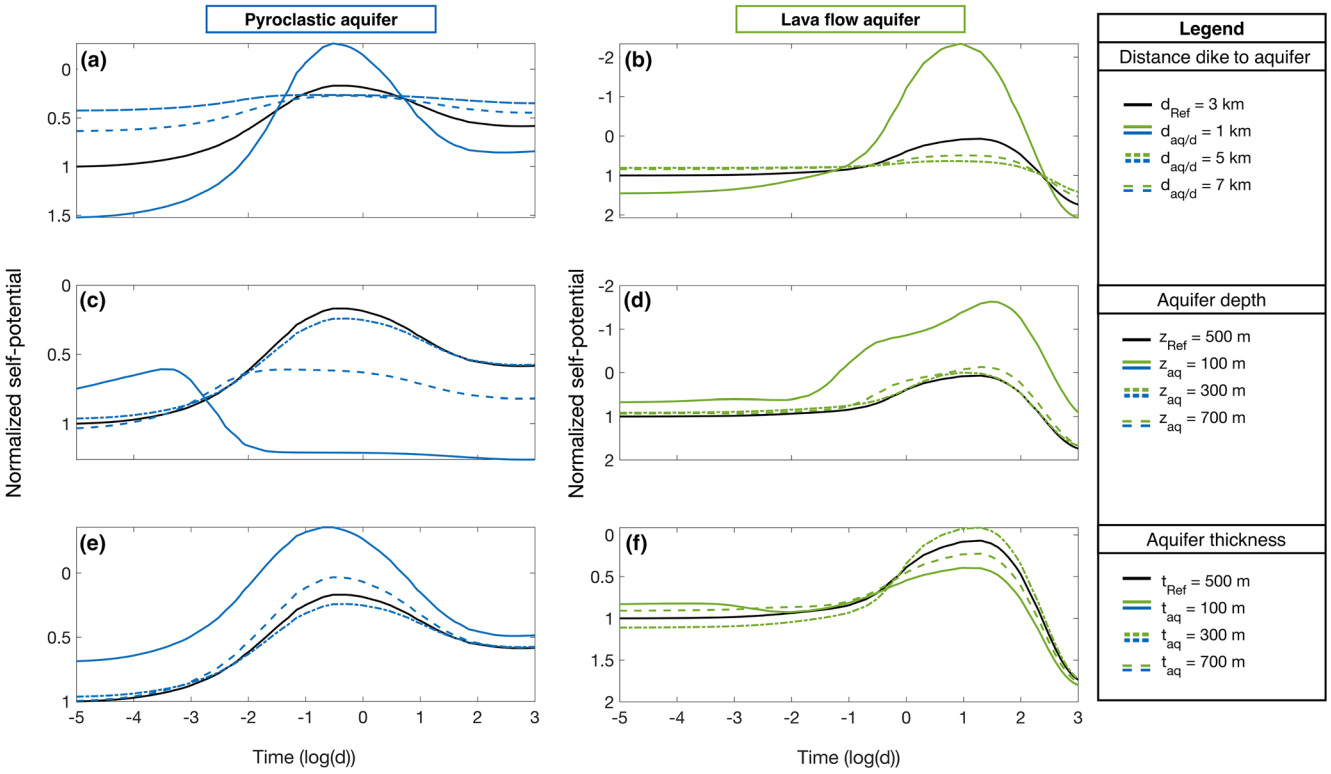

Figure 7. Effect of spatial variation of pressure source and aquifer on the temporal SP evolution (x-axis, log-scale) at the central surface point ($x = z = 0$). Normalized SP is shown in (a) PA, (b) LFA for proximity between dike and aquifer, (c) PA, (d) LFA aquifer depth, and (e) PA, (f) LFA aquifer thickness. All variations provoke changes in magnitude and temporal occurrence of the peak amplitude compared to the reference simulations. SP values are normalized to $SP_{PA} = -22.6$ mV and $SP_{LFA} = -0.35$ mV at $t = 1$ s and are of positive polarity for SP variations < 0 relative to SP_{Ref}. Note, that increasing aquifer depth and thickness shorten the distance between aquifer and pressure source. LFA, lava flow aquifer; PA, pyroclastic aquifer; SP, self-potential.

heated to 200°C in 100 days (slow; heating 1) or 10 days (fast; heating 2). In the heating-study, we notice the greatest deviation in peak amplitude compared to the reference simulation in the LFA model for the case of fast heating. However, absolute SP variations in the LFA model are relatively small. Independent of the heating rate, SP values peak simultaneously within the LFA ($\log(t) \sim 1$ day) and PA model ($\log(t) \sim 0$ days) but are time-shifted compared to their reference simulations.

4. Discussion

4.1. Reference Simulation

Our joint multiphysical approach shows that strain-induced fluid flow produces SP anomalies of detectable amplitude, with a spatial correlation between SP signal and total displacement. Predicted surface displacements in the range of a few to tens of cm are broadly consistent with GPS data recorded during recent dike intrusions (e.g., Bonaccorso et al., 2002; Bonforte et al., 2013; Segall et al., 2001). We observe fundamental spatio-temporal differences in SP amplitude and ground deformation between both reference models for an equivalent source pressurization and model geometry. Elastic properties of the layered crust govern the mechanical response to subsurface stressing and hence surface displacement. As the LFA is much stiffer than the PA, stress and strain attenuation is smaller, resulting in greater surface deformation. These mechanical differences between both models influence the poroelastic response and resulting pore pressure induced electrokinetic process.

The initial pore pressure distribution is governed by the poroelastic response to source pressurization, where dilatational strain correlates with a fall in pore pressure. In both models, the lateral opening of the dike pro-

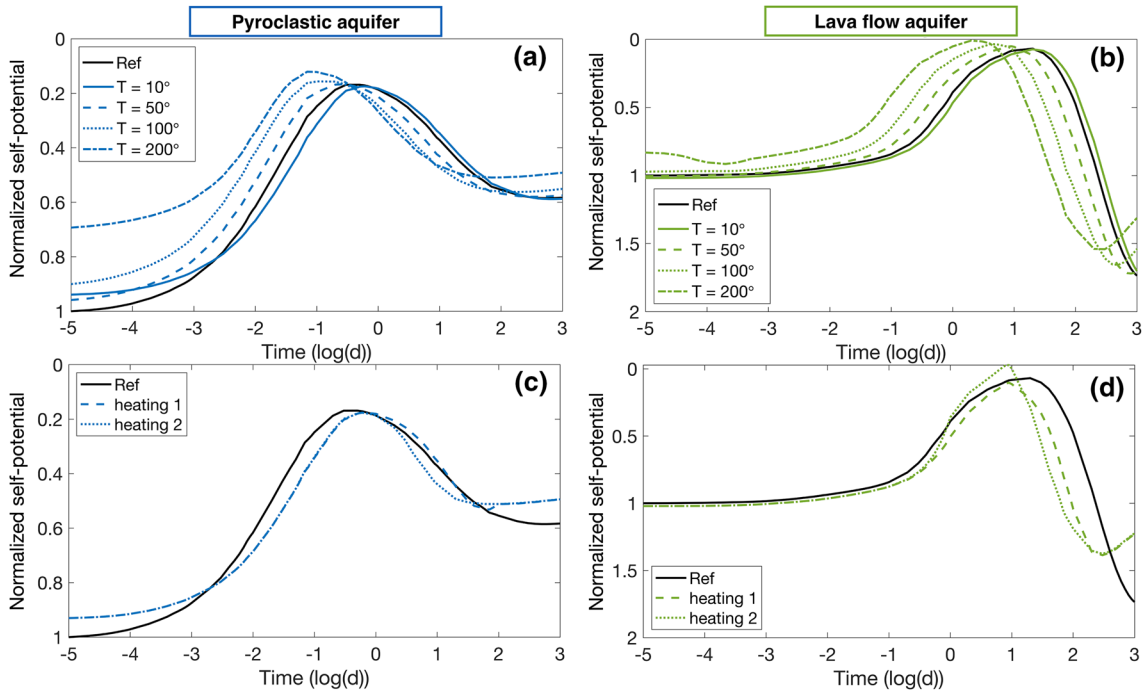

Figure 8. Effect of temperature on SP signal with time at the central surface point ($x = z = 0$) for an individual temperature increase (a and b) and linear heating (c and d). Temperature-dependent fluid properties are changed simultaneously in aquifer and cap rock, while other parameters are kept constant. Heating is accomplished by increasing temperature linearly to 200°C, (i) in 100 days (heating 1) and (ii) in 10 days (heating 2). SP values are normalized to $SP_{PA} = -22.6$ mV and $SP_{LFA} = -0.35$ mV at $t = 1$ s. Temperature and linear heating influence the magnitude and temporal occurrence of the peak amplitude. LFA, lava flow aquifer; PA, pyroclastic aquifer; SP, self-potential.

vokes central dilation in the aquifer and compression close to the free surface (Figure S1). Vertical uplift at 5 km distance provokes dilatational strain in most domains of both models, except for the PA. Here, the stiff cap rock prevents the soft PA from dilating, resulting in compression and a pore pressure rise. Even though pore pressure variations (relative to hydrostatic pressure) are highest in the aquifer of the LFA model, the PA model yields greater superficial SP amplitudes. This might result from the overall higher pore pressures in the PA model, especially in the cap rock, as SP anomalies at the ground surface result from the superposition of electrokinetic processes in aquifer and cap rock. The negative polarity of the central SP anomalies can be explained by the inverse relationship between pore pressure and electrical potential (Equation B4). In groundwater investigations, positive SP anomalies are accompanied by a fall in well-levels (Revil, Naudet et al., 2003; Rizzo et al., 2004) coinciding with SP signals due to pore pressure reduction in areas of dilation in this study.

The temporal evolution of pore pressure and SP signals are governed by strain-induced groundwater flow (Figure S2). Fluid flow is initiated to balance the topographic gradient and spatial pore pressure variations. Pore pressure time series (Figure S1) indicates that fluid-driven equilibration processes are sustained in the cap rock (LFA model) throughout time, while stabilizing in the aquifer (LFA model, $\log(t) \sim 0$ days) and PA model ($\log(t) \sim 2.4$ days). The temporal evolution of SP anomalies perfectly mirror the pore pressure curves in aquifer and cap rock of the PA model. SP signals in the PA reference and no-flow cap rock model (Figure S3b; see Section S.1) equilibrate around the same value. Therefore, we can conclude that electrokinetic processes in the aquifer are the main source of superficial SP variations over time in the PA model. In contrast, SP signals in the LFA model most likely originate from poroelastic processes in the cap rock as pore pressure in the aquifer equilibrates rapidly, but SP variations are protracted. This matches with findings reported by Strehlow et al. (2015) where fluid flow equilibrates in the lava flow aquifer within days. Differences in time-dependent fluid flow and pore pressure variations are governed by the hydraulic domain properties. While the permeable PA is overlain by a less permeable cap rock, the LFA has lower permeability and porosity compared to the overlying cap rock. Therefore, fluid flow in the LFA model occurs predominantly in the cap rock after $\log(t) \sim 0$ days.

Strain-induced fluid flow governs surface deformation with time. While the elasticity of crustal rocks controls the initial mechanical response, poroelasticity of the aquifer and cap rock distorts the displacement field compared to purely elastic mechanics. The spatio-temporal deformation signal deviates strongest relative to the elastic solution in the PA model (Figure S4). This highlights that elastic and poroelastic responses to an initial stress perturbation control the evolution and partitioning of stress and strains in the subsurface, and the amplitude of surface deformation.

4.2. Evaluation of Parameter Space Exploration

The sensitivity analysis allows us to categorize the parameter space into (i) non-influential, (ii) semi-influential, and (iii) influential parameters on superficial SP signals. In terms of domain properties, rock densities are non-influential but 14 domain properties are. Of the elastic parameters Young's modulus and Poisson's ratio influence SP anomalies over time (group iii), as they govern the stress-strain response to the instantaneous pressurization (Equation A4) and fluid-induced pore pressure variations (Equation A2) in the poroelastic domains (cap rock and aquifer). It follows that as long as fluid flow is present with time, elastic parameters govern the poroelastic response and consequently electrokinetic processes. Hydraulic properties show a significant influence up to a few days after dike pressurization (group ii) as they accommodate initial stresses and strains. Relative to elastic and electric parameters, hydraulic properties become negligible with time, except for the cap rocks Biot-Willis coefficient in the LFA model. The influence of α_c (LFA model) with time might be due to fluid flow and poroelastic processes occurring predominantly in the cap rock, or the parameter range chosen for the sensitivity analysis. Electric properties show an influence (group iii) throughout time, which can be expressed by the streaming current coupling coefficient (L_{SP}, Equation B4). As long as the domain is subjected to a pressure gradient, an electrical signal is generated which in turn is controlled by the electrical parameters (σ, C_{SP}).

Our results indicate that cap rock streaming potential coupling coefficients (C_{SPc}) strongly affect the magnitude and temporal evolution of SP anomalies. C_{SP} is a key parameter in hydroelectric processes, determining the strength of coupling between electrical potential and hydraulic gradient (Equation B4). Both in turn govern the SP magnitude. The effect of C_{SPc} on SP signals, together with the sensitivity analysis, highlights that knowledge of subsurface material properties aids the interpretation of observed SP anomalies. Therefore, a priori laboratory measurements of the C_{SPc} magnitude similar to Revil et al., (2008) are beneficial for the evaluation of SP signals.

We show that pore fluid temperatures affect the spatio-temporal SP pattern. In both conceptual models tested in this study, higher SP magnitudes correlate with lower temperatures. The greatest absolute SP deviations compared to the reference simulation are observed in the PA model. While different heating rates yield similar SP peak amplitude in the PA model, peak SP amplitudes for the case of rapid heating deviate from reference values and slow heating in the LFA model. Beside pore fluid parameters, the temperature-dependence of electric properties (σ, C_{SP}) is well known (Ikard & Revil, 2014; Revil et al., 2013). We did not account for electric rock properties in the temperature study, as their sensitivity is assessed during the parametric analysis and precise rock specific temperature-dependent values are scarce. In active hydrothermal areas, where a strong thermal gradient is present, electrical resistivity data can be used to account for the thermal effect and constrain electric parameters (e.g., Finizola et al., 2010; Revil et al., 2008).

4.3. Source Orientation and Distance to Aquifer

We show that pressurization of either a sill or a dike intrusion produces distinguishable spatial SP and ground deformation patterns, provoked by distinct poroelastic and electrokinetic processes. Resultant differences in pore pressure variations induce negative SP polarities at the center of the reference dike model, whereas positive SP signals are attributed to a pressurized sill. Despite the modeled deeper source location of the horizontal intrusion ($z_{sill} = -6.5$ km) SP amplitudes are markedly higher than that produced by the dike intrusion ($z_{dike} = -4$ km). Matching results reported by Strehlow et al. (2015), a fall in hydraulic head/pore pressure caused by the vertical displacement of country rock is observed directly above the dilating sill source. The reduction in pore pressure induces positive SP signals above the pressure source, coinciding

with SP anomalies observed above pumping wells (Revil, Naudet et al., 2003; Rizzo et al., 2004), and hydrothermal systems (volcano-electric effect; Revil, Saracco et al., 2003; Zlotnicki & Nishida, 2003).

Our results indicate that the spatio-temporal behavior of the SP signal in terms of peak amplitudes is dependent on the proximity of the pressure source to the aquifer as well as on aquifer depth and thickness. Highest SP variations relative to the reference values are observed for the greatest proximity between dike and aquifer. These amplified SP signals correlate with higher pore pressures as observed in models by Strehlow et al. (2015) for magma reservoirs located closest to an aquifer, resulting from a larger quantity of strain absorbed by the aquifer. In our study, a thin (100 m thickness) and a shallow-seated (100 m depth) PA generates SP signals that are markedly different in peak amplitude and their temporal behavior compared to reference values. For the same parameter sets, the LFA model produces minor absolute deviations from the reference values. As distance between the dike and aquifer is equivalent for the thinnest and shallow-most aquifer in both models, the same amount of strain is transferred into the aquifer. It follows that SP signals are governed by the aquifer parameterization and equally by the domain properties of the overlying cap rock, whose extent varies along with changes in aquifer thickness and depth.

4.4. Implications for Volcanic Unrest Monitoring

We have shown that SP anomalies can reflect subsurface stressing beneath volcanoes, suggesting that their implementation could be of great value for volcano monitoring efforts. SP measurements are cost-effective, fast (Nyquist & Corry, 2002), and easily applicable in challenging volcanic terrains (Grobbe & Barde-Cabusson, 2019). At several volcanoes, electric precursors have been observed prior to a volcanic crisis (e.g., Friedel et al., 2004; Zlotnicki et al., 2001, 2005) sometimes even before the presence of seismicity and ground deformation (Zlotnicki, 2015, and references therein), indicating that SP signals may provide first insights into volcanic unrest. This might be especially important in areas where non-electric precursors might occur only shortly before an eruption (e.g. at the monogenetic Auckland Volcanic Field; Sherburn et al., 2007) and where unrest is accompanied by protracted ground deformation. As ground displacement and SP patterns show a spatio-temporal correlation, the combination of these methods could become an important component in volcanic unrest monitoring to track the evolution and orientation of a pressurized magmatic intrusion. Joint inversion of geodetic (e.g., Gottsmann, Flynn et al., 2020; Hickey et al., 2015; Montgomery-Brown et al., 2010; Segall et al., 2013) and SP data (e.g., Crespy et al., 2008; Jardani et al., 2008) could be used to characterize the source of volcanic unrest such as its location, shape, and orientation. Mahardika et al. (2012) has shown in a coupled seismoelectric study, that electrical signals can determine seismic events in time and space, and provide additional insights on causative processes compared to seismic data alone. In absence of surface deformation, SP/electrical anomalies might still provide first-order evidence of volcanic unrest, while the combination with other monitoring signals can constrain driving mechanism behind volcanic unrest.

Strain-induced SP anomalies are transient signals on top of the background level. Interpretation of these signals depends on a priori information of background behavior (continuous SP data) and non-volcanic processes that produce SP signals (e.g., meteorological processes). Infiltration of meteoric water or extraction of groundwater for water supply induces well-level fluctuations in aquifers, resulting in seasonal SP variations. Up-to-date meteorological and water table data are essential to assess SP anomalies due to well-level changes. Additionally, a prior geoelectrical and geochemical survey can be used to constrain electrical parameters and identify preferential fluid pathways for rainwater (e.g., Finizola et al., 2002, 2010; Revil et al., 2008, 2011), where electrokinetic processes emerge and superimpose on SP signals from subsurface stressing. Injection of hydrothermal fluids can equally modify SP amplitudes as observed in the temperature study. Upwards migrating hot fluids can produce positive SP anomalies along the ground surface (e.g., Revil, Saracco et al., 2003; Zlotnicki & Nishida, 2003), which is most essential for areas with an inherent active hydrothermal system. All these processes can act either simultaneously or in isolation and need to be considered carefully when assessing strain-induced SP signals.

We model central superficial SP anomalies of −0.35 mV (LFA) to −22.6 mV (PA) in the reference simulations, with values up to −947 mV (PA) and −7.3 mV (LFA) in the parametric analysis. In geothermal and volcanic areas, SP anomalies between a few tens of millivolts to a few volts are widely recognized (e.g.,

Corwin & Hoover, 1979; Fitterman & Corwin, 1982; Zlotnicki & Nishida, 2003). While modeled SP amplitudes in the PA model fall within the range of observed SP anomalies, SP values in the LFA model fall below the lower bound and might only be detectable in a noise-free environment. Resolution of SP/electrical field measurements varies between a few microvolts (Crespy et al., 2008; Zlotnicki, 2015) to 100 microvolts (Grobbe & Barde-Cabusson, 2019; Revil & Jardani, 2013). Repeated SP surveys predominantly focus on identifying changes in hydrothermal activity of active volcanoes, rather than eruption monitoring. However, continuous SP measurements have shown the sensitivity of the technique to monitor changes in volcanic activity. Large SP anomalies characterize volcano-seismic events (Taal; Zlotnicki et al., 2018) as well as variations in fumarolic activity (Merapi; Byrdina et al., 2012). Continuous SP surveillance throughout a volcanic crisis is scarce, but electrical field data resulting from electrokinetic processes exist at Miyake-jima volcano (Zlotnicki, 2015). Here, a sharp spike of 175 mV/km in the horizontal electrical field component accompanied the submarine eruption at Miyake-jima volcano in 2000, which is ∼22 (PA) and ∼250 (LFA) times higher than in our reference simulations. SP signals between −50 and −300 mV were observed along different SP profiles a few weeks prior to the eruption. While SP amplitudes in our reference simulations are relatively small compared to observed values at Miyake-jima volcano, we have shown that SP amplitudes are conditional on input parameters as well as thermal and spatial effects. In reality, signal amplitudes might be higher than predicted in our reference simulations.

4.5. Model Limitations

Our multiphysical modeling approach is exclusively focused on strain-induced electrokinetic effects and thus contains inherent but necessary simplifications. First, we assume a priori water-saturation in both cap rock and aquifer. Time-dependent saturation processes are not studied. Second, we assume homogeneous domain properties throughout the individual layers. In reality, however, spatial heterogeneities exist. Third, our models do not account for topography and associated gradient flow, or seasonal well-level fluctuations. The latter may arise from variations in precipitation or the extraction of groundwater by pumping. Such perturbations are expected to influence the temporal SP pattern. Finally, we consider a single-phase fluid and neglect temperature-dependent phase changes of the pore fluid (e.g., liquid to vapor). While our parametric study has shown that temperature-dependent fluid parameters influence the temporal evolution of the SP signal, we do not consider processes in a system that contains a free-vapor phase such as in a hydrothermal system. Our study is focused on a cold crust scenario and neglects inelastic stress responses due to protracted thermal effects in the subsurface by shallow-seated and long-term magma accommodation. Strong thermal gradients induce an electrical SP resulting from thermoelectric processes, which is superimposed on the streaming potential (Corwin & Hoover, 1979; Fitterman & Corwin, 1982). Here we neglect thermoelectric SP anomalies.

In addition to the electrokinetic effects studied here, SP anomalies in volcanic settings can also arise from electrochemical, thermoelectric and redox-processes (e.g., Zlotnicki & Nishida, 2003) within hydrothermal systems and alteration zones and may need to be quantified separately. Furthermore, SP amplitudes are sensitive to the water-saturation in soils above aquifers (Matsushima et al., 2017) and heterogeneities in subsurface resistivity (e.g., Ishido, 2004). A number of studies show that the streaming potential coupling coefficient depends not only on the water salinity but also on hydraulic rock properties, temperature, pore water conductivity and EDL properties (e.g., Ishido, 2004; Jouniaux & Pozzi, 1995; Jouniaux et al., 2000; Revil, Saracco et al., 2003). Controlled laboratory studies on rock samples from the field area may help to address these contributions.

5. Conclusions

In this study, we have analyzed SP anomalies from strain-induced fluid flow utilizing fully coupled numerical models. We have shown that a pressurized dike and sill intrusion produces substantial and measurable SP signals at the ground surface, which are broadly representative of observations from volcanic areas. Electrokinetic processes are governed by the initial poroelastic response and temporal pore pressure changes by fluid flow due to subsurface strains. Source pressurization and distance between the magmatic intrusion

and the aquifer determine the amplitude of the surface strains, while elasticity governs strain partitioning throughout the crust. The parametric study revealed that the Young's modulus of all domains, together with the streaming potential coupling coefficient and electrical conductivity of aquifer and cap rock, are most influential in controlling the evolution of SP signals with time. In contrast, most hydraulic properties are only significant shortly after source pressurization. SP anomalies and ground deformation signals can be used to deduce source orientation (dike vs. sill), due to their distinct spatial pattern. We have shown that SP anomalies mirror ground deformation patterns and are hence sensitive to subsurface strains (ϵ_{vol} ranging between a few to a few tens of microstrains). Once SP data are corrected for non-volcanic background and seasonal trends by aquifer head changes and rainfall, SP time series should provide valuable insights into pre-eruptive processes, especially when combined with geodetic or other geophysical observations. For example, joint inversions of geodetic and SP time series should help to constrain source properties and driving mechanisms behind volcanic unrest.

Appendix A: Poroelasticity

The underlying physics of poroelasticity is governed by (a) fluid-to-solid coupling by applying an initial pore fluid pressure in solid mechanics and (b) solid-to-fluid coupling in the fluid dynamics (use Biot, 1962; Comsol, 2018; Wang, 2000 for further reading). Poroelasticity is based on the Navier-Stokes equation for solids:

$$-\nabla \cdot \sigma_b = \rho_a \boldsymbol{g}, \tag{A1}$$

where σ_b is the stress tensor and the body force ($F_v = \rho_a \mathbf{g}$), calculated from the average density (ρ_a) of the porous medium and the gravitational acceleration ($\mathbf{g}$) acting on it. The solid is threated as quasistatic, thus inertial forces are neglected. Solid deformation in a poroelastic material obeys Hooke's law of linear elasticity:

$$\sigma_b = \mathbf{C}\epsilon - \alpha p_f \mathbf{I}, \quad \text{with} \quad \mathbf{C} = \mathbf{C}(E,\nu) \tag{A2}$$

which relates the stress tensor (σ_b) with the strain tensor (ϵ). Here, $\mathbf{C}$ is the drained elasticity matrix, which is represented by the Young's modulus (E) and the Poisson's ratio (ν). The term $\alpha\, p_f$ characterizes the fluid-to-solid coupling, with α being the Biot-Willis coefficient, p_f being the pore pressure and $\mathbf{I}$ being the unity matrix. The Biot-Willis coefficient is a key poroelastic property, which relates volumetric strain to pore fluid volume (or pore pressure) and determines the degree of poroelastic response. Values of α range between the materials porosity to 1, approaching 1 for soft media.

Fluid flow in a poroelastic medium is given by Darcy's law, which includes gravity effects:

$$\mathbf{q} = -\frac{\kappa}{\eta_f}\left(\nabla p_f + \rho_f g \nabla Z\right), \tag{A3}$$

and the mass conservation:

$$\rho_f S \frac{\partial p_f}{\partial t} + \nabla \cdot \left(\rho_f \mathbf{q}\right) = Q - \rho_f \alpha \frac{\partial \epsilon_{\text{vol}}}{\partial t}, \tag{A4}$$

where $\mathbf{q}$ is the Darcy velocity, ρ_f is the fluid density, κ is the solid permeability, η_f is the fluid viscosity, Z is the elevation, S is the poroelastic storage, Q is the mass source or sink, and ϵ_{vol} is the volumetric strain. The solid-to-fluid coupling is achieved by linking the volumetric strain rate ($\partial\epsilon_{\text{vol}}/\partial t$) to the fluid modulus. The poroelastic storage is expressed as

$$S = \phi\chi_f + \frac{(\alpha - \phi)(1-\alpha)\left(3(1-2\nu)\right)}{E}, \tag{A5}$$

where ϕ is the porosity of the porous medium and χ_f the compressibility of the fluid.

Appendix B: Self-potential

The constitutive equations describing the electrokinetic phenomena in a fluid-saturated porous media, combines the macroscopic electrical current density with Darcy's velocity (for details see Bolève et al., 2011; Ishido & Mizutani, 1981; Revil, Pezard et al., 1999; Revil, Schwaeger et al.,1999):

$$\mathbf{j}_{SP} = -\sigma\nabla\varphi - \mathbf{J}_{SP}, \tag{B1}$$

where $\mathbf{j}_{SP}$ is the streaming current density, σ is the electrical conductivity of the porous media, φ is the electrical potential, and $\mathbf{J}_{SP}$ is the streaming current density. The continuity equation for electrical charge is given by

$$\nabla \cdot \mathbf{j}_{SP} = 0. \tag{B2}$$

The subscript SP indicates that corresponding mechanisms are of electrokinetic origin. The streaming current density given in Equation B1 can be expressed as

$$\mathbf{J}_{SP} = -L_{SP}\nabla p, \tag{B3}$$

and is sensitive to the fluid pressure gradient characterized by Darcy's law (Equation A3) and to the macroscopic streaming current coupling coefficient L_{SP}. The latter is related to the streaming potential coupling coefficient (C_{SP}) and the electrical conductivity as follows:

$$C_{SP} = \frac{-L_{SP}}{\sigma} = \left(\frac{\delta\varphi}{\delta p}\right)_{J=0} = \frac{\Delta\varphi}{\Delta p}. \tag{B4}$$

C_{SP} is a crucial parameter to quantify hydroelectrical mechanisms, determining the strength of coupling between pore pressure and electrical potential (e.g., Boleve et al., 2011; Revil, Schwaeger et al.,1999).

Appendix C: Sensitivity analysis

For the global sensitivity analysis, a one-at-a-time sampling matrix **B**:

$$\mathbf{B}_{j,k} = \begin{pmatrix} x_{1,1} & x_{1,2} & \cdots & x_{1,k} \\ x_{2,1} & x_{2,2} & \cdots & x_{2,k} \\ \vdots & \vdots & \ddots & \vdots \\ x_{j,1} & x_{j,2} & \cdots & x_{j,k} \end{pmatrix} \tag{C1}$$

is generated from a set of input values (x), where k is the total number of parameters and $j = k+1$ represents an independent model run or row. The sampling matrix **B** is constructed that the first row of each block represents a randomly sampled assembly of parameters, while only one input factor varies in each subsequent row (Morris et al., 1991; Saltello et al., 2008). The final sampling matrix (**X**) is defined as:

$$\mathbf{X}_n = \begin{pmatrix} \mathbf{B}_1 \\ \mathbf{B}_2 \\ \vdots \\ \mathbf{B}_n \end{pmatrix}, \tag{C2}$$

where n is the number of model runs, while the total number of sampling points (rows) or model runs in **X** is $r = n \times j$ (Morris et al., 1991).

We use the Elementary Effect Test (EET; Morris, 1991), which is an efficient and computational reasonable approach for screening the parameter space for negligible input factors. An Elementary Effect EET_i is computed for each model input ($i = 1,...,k$) of the sampling matrix as followed:

$$EET_i = \frac{\left|\mathbf{Y}_{i+1} - \mathbf{Y}_1\right|}{\left|\mathbf{B}i + 1, i - \mathbf{B}_{1,i}\right|}\left(x_{\max_i} - x_{\min_i}\right). \tag{C3}$$

Here $\mathbf{Y}$ is the associated $1 \times j$ output matrix for each model run, while $x_{\max}$ and $x_{\min}$ define the maximal and minimal range of each input factor, respectively. This calculation is repeated for n model runs to obtain n EET ($EET_{n,i}$) for each input parameters (Price et al., 2018). The EET sensitivity can be assessed by the mean, which denotes the degree of influence of an input factor, and the standard deviation, evaluating the interaction between parameters. As we are predominantly interested in the overall influence of the parameter space on the model output, we use the mean value of EET obtained from

$$\mu_i = \frac{1}{n}\sum_{j=1}^{n}\left|EE_i^j\right|. \tag{C4}$$

The upper ($x_{\min}$) and lower ($x_{\max}$) bound of the parameter space can be taken from Table 1.

Data Availability Statement

Comsol Multiphysics (https://uk.comsol.com) and Matlab (https://www.mathworks.com) were used for data modeling and processing. Data informing this manuscript are available from http://zenodo.org (doi: http://doi.org/10.5281/zenodo.3946649). Model source files are available from the corresponding author upon reasonable request.

Acknowledgments
Fee Arens is supported by a NERC GW4+ Doctoral Training Partnership studentship from the Natural Environment Research Council (NERC; NE/L002434/1) and is thankful for the support and additional funding from CASE partner GNS Science and DEVORA. A. Revil and an anonymous reviewer provided constructive and valuable comments which helped to improve the manuscript.

References

Barde-Cabusson, S., Gottsmann, J., Marti, J., Bolos, X., Camacho, A. G., Geyer, A., et al. (2014). Structural control of monogenetic volcanism in the Garrotxa volcanic field (Northeastern Spain) from gravity and self-potential measurements. *Bulletin of Volcanology*, *76*(788), 1–13. https://doi.org/10.1007/s00445-013-0788-0

Biot, M. A. (1962). Mechanics of deformation and acoustic propagation in porous media. *Journal of Applied Physics*, *33*(4), 1482–1498. https://doi.org/10.1063/1.1728759

Boleve, A., Janod, F., Revil, A., Lafon, A., & Fry, J. J. (2011). Localization and quantification of leakages in dams using time-lapse self-potential measurements associated with salt tracer injection. *Journal of Hydrology*, *403*(3–4), 242–252. https://doi.org/10.1016/j.jhydrol.2011.04.008

Bonaccorso, A., Aloisi, M., & Mattia, M. (2002). Dike emplacement forerunning the Etna July 2001 eruption modeled through continuous tilt and GPS data. *Geophysical Research Letters*, *29*(13), 2-1–2-4. https://doi.org/10.1029/2001GL014397

Bonforte, A., Guglielmino, F., & Puglisi, G. (2013). Interaction between magma intrusion and flank dynamics at Mt. Etna in 2008, imaged by integrated dense GPS and DInSAR data. *Geochemistry, Geophysics, Geosystems*, *14*(8), 2818–2835. https://doi.org/10.1002/ggge.20190

Brocher, T. M. (2005). Empirical relations between elastic wavespeeds and density in the Earth's crust. *Bulletin of the Seismological Society of America*, *95*(6), 2081–2092. https://doi.org/10.1785/0120050077

Byrdina, S., Rücker, C., Zimmer, M., Friedel, S., & Serfling, U. (2012). Self-potential signals preceding variations of fumarole activity at Merapi volcano, Central Java. *Journal of Volcanology and Geothermal Research*, *215–216*, 40–47. https://doi.org/10.1016/j.jvolgeores.2011.12.002

Comsol. (2008). *Earth science module* (Tech. Rep. Version 3.5.). COMSOL AB.

Comsol. (2018). *Subsurface flow module user's guide* (Tech. Rep. Version 5.4). COMSOL.

Corwin, R. F., & Hoover, D. B. (1979). The self-potential method in geothermal exploration. *Geophysics*, *44*(2), 226–245. https://doi.org/10.1190/1.1440964

Crespy, A., Revil, A., Linde, N., Byrdina, S., Jardani, A., Boleve, A., & Henry, P. (2008). Detection and localization of hydromechanical disturbances in a sandbox using the self-potential method. *Journal of Geophysical Research*, *113*(1), 1–23. https://doi.org/10.1029/2007JB005042

Delgado, F., Pritchard, M., Samsonov, S., & Cordova, L. (2018). Renewed post-eruptive uplift following the 2011–2012 rhyolitic eruption of Cordon Caulle (Southern Andes, Chile): Evidence for transient episodes of magma reservoir recharge during 2012–2018. *Journal of Geophysical Research: Solid Earth*, *123*(11), 9407–9429. https://doi.org/10.1029/2018JB016240

Fetter, C. W. (2013). *Applied hydrogeology: Pearson New International Edition* (4th ed.). Harlow, UK: Pearson Education Limited.

Finizola, A., Ricci, T., Deiana, R., Cabusson, S. B., Rossi, M., Praticelli, N., et al. (2010). Adventive hydrothermal circulation on Stromboli volcano (Aeolian Islands, Italy) revealed by geophysical and geochemical approaches: Implications for general fluid flow models on volcanoes. *Journal of Volcanology and Geothermal Research*, *196*(1–2), 111–119. http://dx.doi.org/10.1016/jjvolgeores.2010.07.022

Finizola, A., Sortino, F., Lenat, J. F., & Valenza, M. (2002). Fluid circulation at Stromboli volcano (Aeolian Islands, Italy) from self-potential and CO_2 surveys. *Journal of Volcanology and Geothermal Research*, *116*(1–2), 1–18. https://doi.org/10.1016/S0377-0273(01)00327-4

Fitterman, D. V., & Corwin, R. F. (1982). Inversion of self-potential data from the Cerro Prieto geothermal field, Mexico. *Geophysics*, *47*(6), 938–945. https://doi.org/10.1190/1.1441361

Freeze, R. A., & Cherry, J. (1979). *Groundwater*. Englewood Cliffs, NJ: Prentice-Hall.
Friedel, S., Byrdina, S., Jacobs, F., & Zimmer, M. (2004). Self-potential and ground temperature at Merapi volcano prior to its crisis in the rainy season of 2000-2001. *Journal of Volcanology and Geothermal Research*, *134*(3), 149–168. https://doi.org/10.1016/j.jvolgeores.2004.01.006
Gottsmann, J., Biggs, J., Lloyd, R., Biranhu, Y., & Lewi, E. (2020). Ductility and compressibility accommodate high magma flux beneath a silicic continental rift caldera: Insights from Corbetti caldera (Ethiopia). *Geochemistry, Geophysics, Geosystems*, *21*(4), 1–19. https://doi.org/10.1029/2020GC008952
Gottsmann, J., Flynn, M., & Hickey, J. (2020). The transcrustal magma reservoir beneath Soufriere Hills Volcano, Montserrat: Insights from 3-D geodetic inversions. *Geophysical Research Letters*, *47*(20), 1–10. https://doi.org/10.1029/2020gl089239
Gottsmann, J., Komorowski, J.-C., & Barclay, J. (2017). Volcanic unrest and pre-eruptive processes: A hazard and risk perspective. In J. Gottsmann J. Neuberg & B. Scheu (Eds.) *Volcanic unrest: From science to society*, Advances in volcanology, (pp. 1–21). Cham, Switzerland: Springer. https://doi.org/10.1007/11157_2017_19
Grobbe, N., & Barde-Cabusson, S. (2019). Self-potential studies in volcanic environments: A cheap and efficient method for multiscale fluid-flow investigations. *International Journal of Geophysics*, *2019*, 1–19. https://doi.org/10.1155/2019/2985824
Gudmundsson, A. (2011). *Rock fractures in geological processes*, Cambridge, UK: Cambridge University Press. https://doi.org/10.1017/CBO9780511975684
Gudmundsson, A. (2012). Magma chambers: Formation, local stresses, excess pressures, and compartments. *Journal of Volcanology and Geothermal Research*, *237–238*, 19–41. https://doi.org/10.1016/j.jvolgeores.2012.05.015
Hashimoto, T., & Tanaka, Y. (1995). A large self-potential anomaly on Unzen Volcano, Shimabara Peninsula, Kyushu Island, Japan. *Geophysical Research Letters*, *22*(3), 191–194. https://doi.org/10.1029/94GL03077
Head, M., Hickey, J., Gottsmann, J., & Fournier, N. (2019). The influence of viscoelastic crustal rheologies on volcanic ground deformation: Insights from models of pressure and volume change. *Journal of Geophysical Research: Solid Earth*, *124*(8), 8127–8146. https://doi.org/10.1029/2019JB017832
Hickey, J., & Gottsmann, J. (2014). Benchmarking and developing numerical Finite Element models of volcanic deformation. *Journal of Volcanology and Geothermal Research*, *280*, 126–130. https://doi.org/10.1016/j.jvolgeores.2014.05.011
Hickey, J., Gottsmann, J., & Mothes, P. (2015). Estimating volcanic deformation source parameters with a finite element inversion: The 2001-2002 unrest at Cotopaxi volcano, Ecuador. *Journal of Geophysical Research: Solid Earth*, *120*(3), 1473–1486. https://doi.org/10.1002/2014JB011731
Hickey, J., Gottsmann, J., Nakamichi, H., & Iguchi, M. (2016). Thermomechanical controls on magma supply and volcanic deformation: Application to Aira caldera, Japan. *Scientific Reports*, *6*, 1–10. https://doi.org/10.1038/srep32691
Ikard, S. J., & Revil, A. (2014). Self-potential monitoring of a thermal pulse advecting through a preferential flow path. *Journal of Hydrology*, *519*, 34–49. https://doi.org/10.1016/j.jhydrol.2014.07.001
Ishido, T. (2004). Electrokinetic mechanisms for the "W"-shaped self-potential profile on volcanoes. *Geophysical Research Letters*, *31*(15), 1–5. https://doi.org/10.1029/2004GL020409
Ishido, T., & Mizutani, H. (1981). Experimental and theoretical basis of electrokinetic phenomena in rock-water systems and its applications to geophysics. *Journal of Geophysical Research*, *86*(80), 1763–1775. https://doi.org/10.1029/JB086iB03p01763
Jardani, A., Revil, A., Boleve, A., Crespy, A., Dupont, J. P., Barrash, W., & Malama, B. (2007). Tomography of the Darcy velocity from self-potential measurements. *Geophysical Research Letters*, *34*(24), 1–6. https://doi.org/10.1029/2007GL031907
Jardani, A., Revil, A., Boleve, A., & Dupont, J. P. (2008). Three-dimensional inversion of self-potential data used to constrain the pattern of groundwater flow in geothermal fields. *Journal of Geophysical Research*, *113*(B9), 1–22. https://doi.org/10.1029/2007JB005302
Jouniaux, L., Bernard, M. L., Pozzi, J. P., & Zamora, M. (2000). Electrokinetic in rocks: Laboratory measurements in sandstone and volcanic samples. *Physics and Chemistry of the Earth, Part A: Solid Earth and Geodesy*, *25*(4), 329–332. https://doi.org/10.1016/S1464-1895(00)00053-3
Jouniaux, L., & Pozzi, J. P. (1995). Streaming potential and permeability of saturated sandstones under triaxial stress: Consequences for electrotelluric anomalies prior to earthquakes. *Journal of Geophysical Research*, *100*(B6), 197–210. https://doi.org/10.1029/95jb00069.10209
Lisowski, M. (2006). Analytical volcano deformation source models. In P. Blondel (Ed.), *Volcano deformation* (pp. 279–304). Chichester, UK: Springer-Verlag Berlin Heidelberg. https://doi.org/10.1007/978-3-540-49302-0_8
Lowrie, W. (2018). *Geophysics: A very short introduction*. Oxford, UK: Oxford University Press. https://doi.org/10.1093/actrade/9780198792956.001.0001
Magee, C., Stevenson, C. T., Ebmeier, S. K., Keir, D., Hammond, J. O., Gottsmann, J. H., et al. (2018). Magma plumbing systems: A geophysical perspective. *Journal of Petrology*, *59*(6), 1217–1251. https://doi.org/10.1093/petrology/egy064
Mahardika, H., Revil, A., & Jardani, A. (2012). Waveform joint inversion of seismograms and electrograms for moment tensor characterization of fracking events. *Geophysics*, *77*(5), ID23–ID39. https://doi.org/10.1190/geo2012-0019.1
Matsushima, N., Nishi, Y., Onizawa, S., Takakura, S., Hase, H., & Ishido, T. (2017). Self-potential characteristics of the dormant period of Izu-Oshima volcano. *Bulletin of Volcanology*, *79*(12), 1–15. https://doi.org/10.1007/s00445-017-1173-1
Michel, S., & Zlotnicki, J. (1998). Self-potential and magnetic surveying of La Fournaise volcano (Reunion Island): Correlations with faulting, fluid circulation, and eruption. *Journal of Geophysical Research*, *103*(B8), 17845–17857. https://doi.org/10.1029/98JB00607
Miller, C. A., Kang, S. G., Fournier, D., & Hill, G. (2018). Distribution of vapor and condensate in a hydrothermal system: Insights from self-potential inversion at Mount Tongariro, New Zealand. *Geophysical Research Letters*, *45*(16), 8190–8198. https://doi.org/10.1029/2018GL078780
Montgomery-Brown, E. K., Sinnett, D. K., Poland, M., Segall, P., Orr, T., Zebker, H., & Miklius, A. (2010). Geodetic evidence for en echelon dike emplacement and concurrent slow slip during the June 2007 intrusion and eruption at Klauea volcano, Hawaii. *Journal of Geophysical Research*, *115*(B7), 1–15. https://doi.org/10.1029/2009JB006658
Morris, M. D. (1991). Factorial sampling plans for preliminary computational experiments. *Technometrics*, *33*(2), 161–171.
Newhall, C. G., Albano, S. E., Matsumoto, N., & Sandoval, T. (2001). Roles of groundwater in volcanic unrest. *Journal of the Geological Society of the Philippines*, *56*, 69–84.
Nichols, W. D., Shade, P. J., & Hunt, C.D. (1996). *Summary of the Oahu, Hawaii, regional aquifer-system analysis* (Vol. 1412, Tech. Rep. No. A): U.S. Department of the Interior. https://doi.org/10.3133/pp1412A
Nyquist, J. E., & Corry, C. E. (2002). Self-potential: The ugly duckling of environmental geophysics. *The Leading Edge*, *446–451*(5), 1197. https://doi.org/10.1190/1.1481251
Phillipson, G., Sobradelo, R., & Gottsmann, J. (2013). Global volcanic unrest in the 21st century: An analysis of the first decade. *Journal of Volcanology and Geothermal Research*, *264*, 183–196. https://doi.org/10.1016/j.jvolgeores.2013.08.004

Pianosi, F., Sarrazin, F., & Wagener, T. (2015). A Matlab toolbox for global sensitivity analysis. *Environmental Modelling & Software*, *70*, 80–85. https://doi.org/10.1016/j.envsoft.2015.04.009

Price, D. C., Angus, D. A., Garcia, A., Fisher, Q. J., Parsons, S., & Kato, J. (2018). A multimethod Global Sensitivity Analysis to aid the calibration of geomechanical models via time-lapse seismic data. *Geophysical Journal International*, *212*(3), 2031–2046. https://doi.org/10.1093/gji/ggx516

Revil, A. (2007). Thermodynamics of ions and water transport in porous media. *Journal of Colloid and Interface Science*, *307*(1), 254–264. https://doi.org/10.1016/j.jcis.2006.10.074

Revil, A., Finizola, A., Piscitelli, S., Rizzo, E., Ricci, T., Crespy, A., & Suski, B. (2008). Inner structure of La Fossa di Vulcano (Vulcano Island, southern Tyrrhenian Sea Italy) revealed by high-resolution electric resistivity tomography coupled with self-potential, temperature, and CO2 diffuse degassing measurements. *Journal of Geophysical Research*, *113*(B7), 1–21. https://doi.org/10.1029/2007JB005394

Revil, A., Finizola, A., Ricci, T., Delcher, E., Peltier, A., Barde-Cabusson, S., et al. (2011). Hydrogeology of Stromboli volcano, Aeolian Islands (Italy) from the interpretation of resistivity tomograms, self-potential, soil temperature and soil CO2 concentration measurements. *Geophysical Journal International*, *186*(3), 1078–1094. https://doi.org/10.1111/j.1365-246X.2011.05112.x

Revil, A., & Florsch, N. (2010). Determination of permeability from spectral induced polarization in granular media. *Geophysical Journal International*, *181*(3), 1480–1498. https://doi.org/10.1111/j.1365-246X.2010.04573.x

Revil, A., & Jardani, A. (2013). Fundamentals of the self-potential method. In *The Self-Potential Method: Theory and Applications in Environmental Geosciences* (pp. 1–22). Cambridge, UK: Cambridge University Press. https://doi.org/10.1017/cbo9781139094252.009

Revil, A., Karaoulis, M., Johnson, T., & Kemna, A. (2012). Review: Some low- frequency electrical methods for subsurface characterization and monitoring in hydrogeology. *Hydrogeology Journal*, *20*, 617–658. https://doi.org/10.1007/s10040-011-0819-x

Revil, A., Karaoulis, M., Srivastava, S., & Byrdina, S. (2013). Thermoelectric self- potential and resistivity data localize the burning front of underground coal fires. *Geophysics*, *78*(5), B259–B273. https://doi.org/10.1190/GE02013-0013.1

Revil, A., & Mahardika, H. (2013). Coupled hydromechanical and electromagnetic disturbances in unsaturated porous materials. *Water Resources Research*, *49*(2), 744–766. https://doi.org/10.1002/wrcr.20092

Revil, A., Naudet, V., Nouzaret, J., & Pessel, M. (2003). Principles of electrography applied to self-potential electrokinetic sources and hydrogeological applications. *Water Resources Research*, *39*(5), 1114. https://doi.org/10.1029/2001WR000916

Revil, A., Pezard, P. A., & Glover, P. W. J. (1999). Streaming potential in porous media: 1. Theory of the zeta potential. *Journal of Geophysical Research: Solid Earth*, *104*(B9), 20021–20031. https://doi.org/10.1029/1999jb900089

Revil, A., Saracco, G., & Labazuy, P. (2003). The volcano-electric effect. *Journal of Geophysical Research*, *108*(B5), 5-1–5-20. https://doi.org/10.1029/2002jb001835

Revil, A., Schwaeger, H., Cathles, L. M., & Manhardt, P. D. (1999). Streaming potential in porous media: 2. Theory and application to geothermal systems. *Journal of Geophysical Research*, *104*(B9), 20033–20048. https://doi.org/10.1029/1999jb900090

Rizzo, E., Suski, B., Revil, A., Straface, S., & Troisi, S. (2004). Self-potential signals associated with pumping tests experiments. *Journal of Geophysical Research*, *109*(B10), 1–14. https://doi.org/10.1029/2004JB003049

Saltello, A., Ratto, M., Andres, T., Campolongo, F., Cariboni, J., Gatelli, D., et al. (2008). *Global sensitivity analysis. The primer*, Chichester, England: John Wiley & Sons, Ltd.

Salvage, R., Karl, S., & Neuberg, J. (2017). Volcano seismology: Detecting unrest in wiggly lines. In J. Gottsmann J. Neuberg & B. Scheu (Eds.), *Volcanic unrest: From science to society*, Advances in Volcanology, (pp. 185–201). Cham, Switzerland: Springer. https://doi.org/10.1007/11157

Schön, J. H. (2011). Physical properties of rocks (Vol. 8), Oxford, UK: Elsevier.

Segall, P., Cervelli, P., Owen, S., Lisowski, M., & Miklius, A. (2001). Constraints on dike propagation from continuous GPS measurements. *Journal of Geophysical Research*, *106*(B9), 19301–19317. https://doi.org/10.1029/2001jb000229

Segall, P., Llenos, A. L., Yun, S. H., Bradley, A. M., & Syracuse, E. M. (2013). Time-dependent dike propagation from joint inversion of seismicity and deformation data. *Journal of Geophysical Research: Solid Earth*, *118*(11), 5785–5804. https://doi.org/10.1002/2013JB010251

Sherburn, S., Scott, B. J., Olsen, J., & Miller, C. (2007). Monitoring seismic precursors to an eruption from the Auckland Volcanic Field, New Zealand. *New Zealand Journal of Geology and Geophysics*, *50*(1), 1–11. https://doi.org/10.1080/00288300709509814

Shibata, T., & Akita, F. (2001). Precursory changes in well water level prior to the March, 2000 eruption of Usu volcano, Japan. *Geophysical Research Letters*, *28*(9), 1799–1802. https://doi.org/10.1029/2000GL012467

Sill, W. R. (1983). Self-potential modeling from primary flows. *Geophysics*, *48*(1), 76–86. https://doi.org/10.1190/1.1441409

Sparks, R. S. (2003). Forecasting volcanic eruptions. *Earth and Planetary Science Letters*, *210*(1–2), 1–15. https://doi.org/10.1016/S0012-821X(03)00124-9

Sparks, R. S., Biggs, J., & Neuberg, J. W. (2012). Monitoring volcanoes. *Science*, *335*, 1310–1311. https://doi.org/10.1126/science.1219485

Steam97Web. (2020). *Steam tables calculator* (Vol. Steam97Web v8.0). MegaWat-Soft Inc. Retrieved from https://www.megawatsoft.com

Strehlow, K., Gottsmann, J. H., & Rust, A. C. (2015). Poroelastic responses of confined aquifers to subsurface strain and their use for volcano monitoring. *Solid Earth*, *6*(4), 1207–1229. https://doi.org/10.5194/se-6-1207-2015

Telford, W., Geldart, L., & Sheriff, R. (1990). *Applied geophysics*. Cambridge, UK: Cambridge University Press.

Turcotte, D. L., & Schubert, G. (2002). *Geodynamics* (2nd ed.). Cambridge, UK: Cambridge University Press. https://doi.org/10.1017/CB09780511807442

USGS. (2018). *Saline water and salinity*. Retrieved from https://www.usgs.gov/special-topic/water-science-school/science/saline-water-and-salinity?qt-science_center_objects=0#qt-science_center_objects

Villasante-Marcos, V., Finizola, A., Abella, R., Barde-Cabusson, S., Blanco, M. J., Brenes, B., et al. (2014). Hydrothermal system of Central Tenerife Volcanic Complex, Canary Islands (Spain), inferred from self-potential measurements. *Journal of Volcanology and Geothermal Research*, *272*, 59–77. https://doi.org/10.1016/j.jvolgeores.2013.12.007

Vinogradov, J., Jaafar, M. Z., & Jackson, M. D. (2010). Measurement of streaming potential coupling coefficient in sandstones saturated with natural and artificial brines at high salinity. *Journal of Geophysical Research*, *115*(B12), 1–18. https://doi.org/10.1029/2010JB007593

Wang, H. F. (2000). *Theory of linear poroelasticity with applications to geomechanics and hydrogeology*, Princeton, NJ: Princeton University Press.

Zlotnicki, J. (2015). Dynamics of volcanic eruptions: Understanding electric signatures for activity monitoring. *Comptes Rendus Geoscience*, *347*(3), 112–123. https://doi.org/10.1016/j.crte.2015.05.003

Zlotnicki, J., Le Mouel, J. L., Gvishiani, A., Agayan, S., Mikhailov, V., Bogoutdinov, S., et al. (2005). Automatic fuzzy-logic recognition of anomalous activity on long geophysical records: Application to electric signals associated with the volcanic activity of La Fournaise volcano (Reunion Island). *Earth and Planetary Science Letters*, *234*(1–2), 261–278. https://doi.org/10.1016/j.epsl.2005.01.040

Zlotnicki, J., Le Mouel, J. L., Sasai, Y., Yvetot, P., & Ardisson, M. H. (2001). Self-potential changes associated with volcanic activity. Short-term signals associated with March 9, 1998 eruption on La Fournaise volcano (Reunion Island). *Annals of Geophysics*, *44*(2), 335–354. https://doi.org/10.4401/ag-3600

Zlotnicki, J., & Nishida, Y. (2003). Review on morphological insights of self- potential anomalies on volcanoes. *Surveys in Geophysics*, *24*, 291–338. https://doi.org/10.1023/B:GEOP.0000004188.67923.ac

Zlotnicki, J., Sasai, Y., Johnston, M. J., Fauquet, F., Villacorte, E., & Cordon, J. M. (2018). The 2010 seismovolcanic crisis at Taal Volcano (Philippines). *Earth Planets and Space*, *70*(1), 1–23. https://doi.org/10.1186/s40623-018-0925-2